UC Berkeley
UC Berkeley Previously Published Works

Title

Electrochemical trapping of metastable Mn^{3+} ions for activation of MnO_2 oxygen evolution catalysts.

Permalink

Journal

ISSN

Authors

Morgan Chan, Zamyla
Kitchaev, Daniil A
Nelson Weker, Johanna
et al.

Publication Date

DOI

Peer reviewed

Electrochemical trapping of metastable Mn³⁺ ions for activation of MnO₂ oxygen evolution catalysts

Zamyla Morgan Chan[a], Daniil A. Kitchaev[b], Johanna Nelson Weker[c], Christoph Schnedermann[a], Kipil Lim[c,d], Gerbrand Ceder[b,e,f,1], William Tumas[g,1], Michael F. Toney[c,1], and Daniel G. Nocera[a,1]

[a]Department of Chemistry and Chemical Biology, Harvard University, Cambridge, MA 02138; [b]Department of Materials Science and Engineering, Massachusetts Institute of Technology, Cambridge, MA 02139; [c]Stanford Synchrotron Radiation Lightsource, SLAC National Accelerator Laboratory, Menlo Park, CA 94025; [d]Department of Materials Science, Stanford University, Menlo Park, CA 94025; [e]Materials Science Division, Lawrence Berkeley National Laboratory, Berkeley, CA 94720; [f]Department of Materials Science and Engineering, University of California, Berkeley, CA 94720; and [g]National Renewable Energy Laboratory, Golden, CO 80401

Electrodeposited manganese oxide films are promising catalysts for promoting the oxygen evolution reaction (OER), especially in acidic solutions. The activity of these catalysts is known to be enhanced by the introduction of Mn³⁺. We present in situ electrochemical and X-ray absorption spectroscopic studies, which reveal that Mn³⁺ may be introduced into MnO₂ by an electrochemically induced comproportionation reaction with Mn²⁺ and that Mn³⁺ persists in OER active films. Extended X-ray absorption fine structure (EXAFS) spectra of the Mn³⁺-activated films indicate a decrease in the Mn–O coordination number, and Raman microspectroscopy reveals the presence of distorted Mn–O environments. Computational studies show that Mn³⁺ is kinetically trapped in tetrahedral sites and in a fully oxidized structure, consistent with the reduction of coordination number observed in EXAFS. Although in a reduced state, computation shows that Mn³⁺ states are stabilized relative to those of oxygen and that the highest occupied molecular orbital (HOMO) is thus dominated by oxygen states. Furthermore, the Mn³⁺(T_d) induces local strain on the oxide sublattice as observed in Raman spectra and results in a reduced gap between the HOMO and the lowest unoccupied molecular orbital (LUMO). The confluence of a reduced HOMO–LUMO gap and oxygen-based HOMO results in the facilitation of OER on the application of anodic potentials to the δ-MnO₂ polymorph incorporating Mn³⁺ ions.

manganese oxide | polymorph | water splitting | catalysis | renewable energy storage

The widespread implementation of solar energy at the level needed for global energy demand (1, 2) requires its efficient storage in the form of fuels (3). The conversion of water to H₂ and O₂ is one of the most energy-dense carbon-neutral fuel schemes to store solar energy (4). Effective catalysts for the hydrogen evolution reaction and oxygen evolution reaction (OER) require a design that manages the coupling of electrons and protons so as to avoid high energy intermediates (5, 6). Of these two proton-coupled electron transfer reactions, the OER is more kinetically challenging, because it requires the management of four electrons and four protons. Oxidic catalysts of cobalt (7–11), nickel (12–16), manganese (17, 18), and other noncritical metals (19, 20) allow OER to be performed efficiently under a wide range of conditions, including nonbasic solutions, where self-healing circumvents corrosion of the catalysts (21). The manganese oxidic OER catalysts are unique, as they are distinguished by their ability to perform OER in acid (17, 18, 22–28). As clearly established by the work of Dismukes and coworkers (29, 30), the OER activity of MnO₂ polymorphs is greatly enhanced when Mn³⁺ ions are present in the lattice (31). Mn³⁺ ions may be introduced by cycling the potential of birnessite-like MnO₂ polymorphs (32, 33). Alternatively, Mn³⁺ ions may be introduced chemically by using the comproportionation of MnO₂ with Mn(OH)₂ to produce a hausmannite-like

intermediate (α-Mn₃O₄) (17). On reoxidation of these films back to a predominantly MnO₂ state, ex situ X-ray photoelectron spectroscopy (XPS) studies indicate an average Mn oxidation state from +3.6 to +3.8 instead of the expected +4.0 of MnO₂, which is consistent with the presence of Mn³⁺ (32, 33). Despite the observation that electrochemical doping of Mn³⁺ enhances OER activity of MnO₂ polymorphs, the role of Mn³⁺ in such electroactivated films is not understood, and it is also not understood why such a reduced state would persist under oxidizing conditions.

X-ray absorption spectroscopy (XAS) measurements made during the electroactivation of electrochemically deposited δ-MnO₂ phase show that Mn³⁺ character remains present in OER active catalyst films and that the Mn–O bond coordination number is lowered with the formation of Mn³⁺. Computational studies, supported by extended X-ray absorption fine structure (EXAFS) results, reveal that the Mn³⁺ ions are located in a tetrahedral environment, which is kinetically stable and induces local strain of the lattice that is observed in Raman microspectroscopic spectra. This strain results in a raising of the O2p valence band above the Mn³⁺ tetrahedral (T_d) and Mn⁴⁺ octahedral (O_h) valence bands with a commensurate lowering of the metal-based conduction bands. Oxidation of tetrahedral Mn³⁺ is

Significance

Manganese oxide films are desirable oxygen evolution reaction (OER) catalysts due to their stability in acidic solutions and viability as earth-abundant materials. Enhanced catalytic activity of MnO₂ incorporated with Mn³⁺ provides an imperative for understanding the structural and electronic effects giving rise to the superior OER catalysis. We show that (*i*) Mn³⁺ is stabilized kinetically in tetrahedral sites and (*ii*) its presence strains the oxide lattice, leading to a favorable disposition of oxide-based vs. metal-based energy levels that favors enhanced OER activity. The results herein offer a design concept of exploiting ion-induced lattice strain for creating superior metal oxide OER catalysts.

thus more difficult than that of oxygen. The studies herein rationalize why Mn^{3+} is observed to persist at the onset of OER in MnO$_2$ polymorphs and why the presence of Mn^{3+} enhances OER catalysis.

Experimental Procedures

Electrochemistry. MnO$_2$ films were prepared following identical procedures as previous studies on these electrodeposited catalysts, and their chemical composition, XPS, EM, and X-ray spectra properties were identical to those of the previously reported material (17, 18, 22). MnO$_2$ films were electrodeposited in solutions containing 0.5 mM Mn^{2+} (prepared from MnCl$_2$·4H$_2$O, 99.995% trace metal basis; Strem) and 0.9 M KNO$_3$ (99.0–100.5%; Macron) at pH 8.0. Powder X-ray diffraction patterns of the amorphous films are well-defined and show that films are locally the MnO$_2$ polymorph of birnessite (δ-MnO$_2$). The electrodeposition protocol ("anodic deposition") for producing δ-MnO$_2$ entailed the application of a constant potential of 1.1 V [vs. normal hydrogen electrode (NHE)] to the electrode. Potentials were converted to the NHE scale by the following relation: $E_{NHE} = E_{Ag/AgCl} + 0.197$ V. All Fluorinated Tin Oxide (FTO) films were sonicated in acetone and rinsed with type I water before use. The MnO$_2$ films activated with Mn^{3+} (generally designated as δ-MnO$_2$^{act}) were generated by multipotential steps ("multistep deposition"), where the electrode was initially held at 1.1 V for 3 s followed by the application of −0.4 V for 2 s, and this multipotential two-step series was repeated as desired. Cyclic voltammograms (CVs) were recorded using a CH Instruments potentiostat. A three-electrode cell configuration was used with a platinum mesh counterelectrode, an Ag/AgCl reference electrode, and an FTO working electrode. The FTO working electrode was sonicated in acetone and rinsed with water before each measurement. The ohmic drop of cell was compensated by using the positive feedback compensation implemented in the instrument.

The electrochemical setup for in situ XAS experiments used a Biologic SP-150 potentiostat in a three-electrode configuration. *SI Appendix*, Fig. S1 presents the geometry and dimensions of the cell used for XAS measurement. The 25 × 25 × ~50-mm quartz cell consisted of three GL14 glass threaded necks (Adams & Chittenden Scientific Glass). A 5-mm hole was cut and fire-polished on one long face of the cell so that the X-ray beam could enter the cell and strike the working electrode surface. Optically transparent 128-μm-thick Polyethylene Terephthalate tape coated with a thin layer (Eastman Chemical Inc.) of conductive Indium Tin Oxide (ITO) was used as the working electrode, which is transparent to X-rays. The Polyethylene Terephthalate–ITO tape was sonicated in acetone and rinsed with type I water before being sealed to the outside of the fire-polished opening of the quartz cell with Devcon 5-min epoxy. An Ag/AgCl reference electrode (BASi; filled with saturated KCl) and a Pt mesh (99.9%; Alfa Aesar) auxiliary electrode were introduced through separate GL14 caps and septa. All experiments were conducted at ambient temperature (~23 °C) and used automatic internal resistance compensation, where the electrode/solution resistance was determined by applying a small potential step at the open circuit potential.

XAS. XAS measurements were conducted at beamline 4–1, Stanford Synchrotron Radiation Lightsource. Measurements were performed at the Mn K edge in a fluorescence geometry using a 30-element solid-state germanium detector. Because the in situ cell is completely absorbing, standard simultaneous energy calibration could not be performed. Instead, a Kapton foil was placed at an angle in front of the first ion chamber to scatter X-rays off-axis. An Mn reference foil and photodiode were used for simultaneous energy calibration using the scattered X-rays. The alignment of the working electrode was optimized after an initial anodic deposition of δ-MnO$_2$ film on the electrode. In situ XAS data were collected continuously during the initial deposition of δ-MnO$_2$ and subsequent activation of the film by multistep activation protocols. During multistep deposition, the two-step potential series was repeated 25 times, which we designate one multistep cycle (one multistep cycle of 25 steps is designated *c1*, two cycles as *c2*, etc.). Each cycle ended at an anodic potential of 1.1 V (one cycle ending on an anodic pulse is designated *c1A*, etc.) or at a cathodic potential of −0.4 V (one cycle ending on a cathodic pulse is designated *c1C*, etc.). A full XAS was collected to a wavenumber, k, of 12 Å^{-1}. Data processing and analysis were conducted using ATHENA and ARTEMIS, part of the IFEFFIT software suite (34). All spectra were calibrated, normalized, and background-subtracted per the protocols outlined in the ATHENA documentation (35). EXAFS data were fit to a birnessite reference to a k window of 3–10.5 Å^{-1}, with single scattering pathways. Given that the establishment of the local

structure of the anodically deposited films is birnessite (22), EXAFS spectra of an anodically deposited film were fit with the assumption of a first shell (Mn–O) coordination number of N$_1$ = 6, yielding an experimental value of 5.3. This lower coordination number for the anodically deposited film was owing to deposition of an amorphous birnessite film and the presence of water in the interlayer. Using the S$_0$^{2} value from an anodically deposited film, a calibration factor was used to obtain the coordination number from the fitted parameters of multicycled films.

Raman Spectroscopy. Raman microspectroscopy was carried out at the Center for Nanoscale Systems on a Horiba LabRam Evolution system using an excitation wavelength of 532 nm (0.5 mW) and a long working distance objective (Olympus LMPLANFL 50×) with a numerical aperture of 0.5, resulting in a Gaussian excitation profile of ~500 nm (FWHM). To average out morphological irregularities, each sample was measured at 49 different locations (55–1,765 cm^{-1}, 15-s integration time, one window, two accumulations) evenly arranged on a square grid of 60 × 60 μm^2. The confocal pinhole was set to 200 μm during the acquisition. Spectra were calibrated to a silicon reference sample (520.64 cm^{-1}), and each spectrum was recorded with a frequency resolution of ~1.7 cm^{-1}. Raw spectra were averaged, multiplied by the Bose–Einstein factor (T = 298 K), baseline-corrected, and fitted to a sum of Lorentzian functions using an unconstrained nonlinear Levenberg–Marquardt optimization algorithm implemented in Labview.

Samples of δ-MnO$_2$ were electrodeposited onto an FTO working electrode by passing a current of 60 mC/cm^2, giving rise to an absorbance of 0.85 at 532 nm; subsequent activation to δ-MnO$_2$^{act} produced a film with an absorbance of 0.73 at 532 nm (*SI Appendix*, Fig. S2).

Calculations. To characterize the electronic structure of the δ-MnO$_2$/δ-MnO$_2$^{act} (referred to as MnOx), in particular focusing on accurately reproducing the relative energy levels of the transition metal and oxygen states, we relied on hybrid density functional theory calibrated using the GW approximation (36). This methodology has been recently reported to accurately reproduce the properties of insulators (37) with mixed Mott–Hubbard and charge–transfer behavior, such as the MnOx system at hand. Specifically, we calibrated the fraction of exact Hartree–Fock exchange, α$_{EX}$, introduced into an Heyd–Scuseria–Ernzerhof type hybrid exchange–correlation functional (38) to reproduce the Kohn–Sham gap obtained from a G$_0$W$_0$ calculation:

$$E_{XC} = (1 - \alpha_{EX})E_x^{PBE} + \alpha_{EX}E_x^{HF} + E_c^{PBE},$$ **[1]**

where E_{XC} is the exchange–correlation energy and PBE refers to the Perdew–Burke–Ernzerhof exchange–correlation functional (39). An exact exchange fraction value of α$_{EX}$ = 0.35 was chosen based on a band gap of α-Mn$_3$O$_4$ (hausmannite) computed in G$_0$W$_0$ to be 3.0 eV, which is in reasonable agreement with previous calculations (40) and experiment (41–43). By calibrating to α-Mn$_3$O$_4$, we sought to capture the behavior of both tetrahedrally and octahedrally coordinated Mn, which are present in this structure. We note that the value obtained by calibration to the birnessite-type MnOOH is also α$_{EX}$ = 0.35, while that obtained by calibration to the experimental band gap of α-Mn$_3$O$_4$ or the purely octahedral birnessite δ-MnO$_2$ structure is α$_{EX}$ = 0.29. This difference, however, does not lead to any qualitative changes in the calculation outcomes to the best of our knowledge. All calibration curves are available in *SI Appendix*, Fig. S3.

A hausmannite (α-Mn$_3$O$_4$) structure was used as a model to investigate the redox behavior of mixed tetrahedrally and octahedrally coordinated Mn within an oxide sublattice. Hausmannite contains both octahedral and tetrahedral Mn environments and is a faithful analog of δ-MnO$_2$^{act} inasmuch as it is generated by oxidizing hausmannite, which is an overlayer on birnessite nanoparticles (22). A computational methodology previously reported for identifying defect-induced redox behavior in transition metal semiconductors was followed (44, 45). (*i*) Beginning with the α-Mn$_3$O$_4$ structure, electrons were removed from the system one by one, compensating for the charge with a homogeneous jellium background and allowing the system to locally relax while keeping the overall lattice fixed. (*ii*) The oxidation states of the Mn and O atoms in the system were then tracked by tracing the evolution of their magnetic moment, which is a precise signature of Mn^{2+}, Mn^{3+}, and Mn^{4+} as well as O^{2-} and O$^-$, as calibrated to typical values observed in known manganese oxide and oxyhydroxide structures. Note that we do not observe relaxation by peroxide formation as evidenced by a lack of short O–O bonds.

All first principles calculations are performed using the Vienna Ab-Initio Simulation Package (46) using the projector-augmented wave method (47), a reciprocal space discretization of 15 Å^{-1}, and a plane-wave cutoff of 650 eV. All calculations are converged to 0.01 eV Å^{-1} on forces and 10^{-8} eV

on total energy to ensure that a reliable minimum is found. Structural models for Mn_3O_4 as well as MnO_2 and $MnOOH$ used in the calibration are obtained from the Inorganic Crystal Structure Database (48), with magnetic orderings chosen based on small supercell enumerations as suggested by previous benchmarks for the MnO_2 system (49).

Results

Electrochemistry. Fig. 1 shows the CVs of as-deposited δ-MnO_2 and δ-MnO_2^{act} films over a potential window that includes OER activity and/or film activation. For all CVs, the bare FTO electrode was first held at open circuit potential, and scans were initiated to positive potentials at a rate of 100 mV/s. Fig. 1A shows the CV for the OER activity of δ-MnO_2 in the absence of Mn^{3+} incorporation. Two notable features are observed, indicated by waves A and B. Wave A corresponds to the nucleation and deposition of δ-MnO_2 from Mn^{2+} as described by the half-reaction (18):

$$A: Mn^{2+} + 2H_2O \rightleftharpoons MnO_2 + 4H^+ + 2e^-. \qquad [2]$$
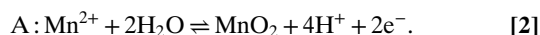
A limiting film thickness is obtained on the initial scan (Fig. 1A, red trace), as there is little subsequent growth on a subsequent scanning (Fig. 1A, blue trace). Wave B corresponds to the modest OER activity of birnessite:

$$B: 2\ H_2O \rightleftharpoons O_2 + 4H^+ + 4e^-. \qquad [3]$$
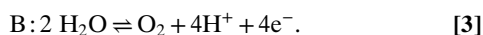
The second scan (Fig. 1A, blue trace) shows that the OER activity for wave B remains effectively unchanged; the OER activity does not change even after 200 scans over a potential window of 1.7–0.5 V (*SI Appendix*, Fig. S4).

Fig. 1B shows the CV of a film that incorporates Mn^{3+} ions by scanning cathodically to potentials of −0.4 V. Wave C corresponds to the comproportionation reaction between Mn^{4+} and Mn^{2+} to produce α-Mn_3O_4 (hausmannite) (22, 33):

$$C: δ\text{-}Mn^{IV}O_2 + 2Mn^{II}(OH)_2 \rightarrow α\text{-}Mn_3^{II,III}O_4 + 2H_2O. \qquad [4]$$
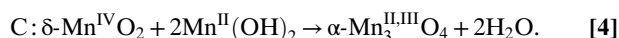
The addition of NO_3^- as a supporting electrolyte is needed for the incorporation of Mn^{3+} ions in the film. Under cathodic potentials, NO_3^- is reduced, forming hydroxide anions at the electrode surface (50), driving the production of $Mn(OH)_2$, and enabling comproportionation to occur. In the absence of Mn^{2+}, Mn^{3+} cannot be produced, and film activation does not occur (17). No appreciable increase in OER activity is observed when an electrodeposited δ-MnO_2 film is scanned to the same limiting cathodic potential in Fig. 1B in the absence of Mn^{2+} (but in the
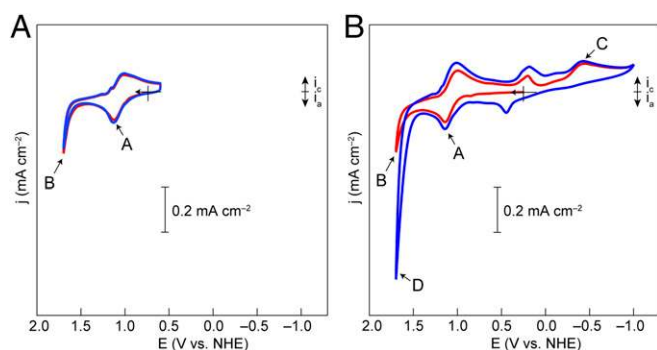

Fig. 1. CVs of a 1-cm² FTO electrode in 0.5 mM Mn^{2+} and 0.9 M KNO_3 solution at 100-mV/s scan rate showing the first (red line) and second (blue line) cycles for (*A*) the as-deposited δ-MnO_2 and (*B*) the as-deposited film activated via the incorporation of Mn^{3+} ions by the comproportionation reaction (Eq. 4). A–D indicate the waves discussed in the text.
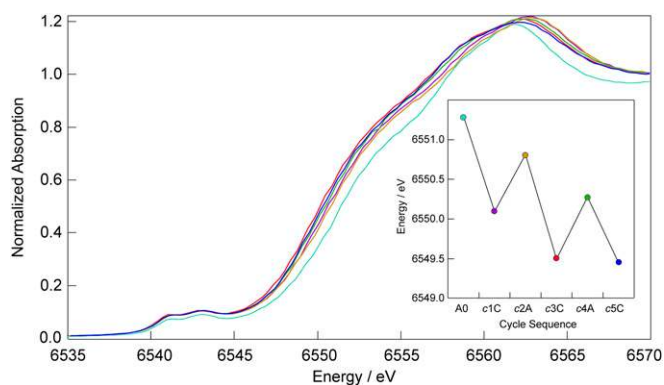

Fig. 2. In situ XANES spectra of an as-deposited δ-MnO_2 film subject to multipotential step activation. XANES spectra were collected after applying a potential between 1.1 and −0.4 V 25 times with a cycle terminating at the anodic or cathodic potential. One cycle (designated c) = 25 steps. The cycle number is designated numerically, and A and C denote cycles terminating at anodic or cathodic potential, respectively. *Inset* shows the energy position of the XANES edge determined from the inflection point as deduced from the maximum of the first derivative. The edge positions in *Inset* are color-coded to match the XANES spectra for cycles A0 (teal), c1C (purple), c2A (orange), c3C (red), c4A (green), and c5C (blue). The normalized absorption was determined from the full spectra shown in *SI Appendix*, Fig. S5.

presence of NO_3^- and OH^-). After inducing the comproportionation reaction on cathodic scanning, the return trace shows a significant increase in current associated with OER (wave D corresponding to Eq. 3), which is indicative of an activated film produced on Mn^{3+} incorporation (denoted δ-MnO_2^{act}). As previously reported (22), the chemistry described by Eq. 4 occurs at the surface of nanosized domains of birnessite, and while there is a predominant birnessite phase, the δ-MnO_2^{act} surface overlayer is unique in that it is the active catalyst for OER.

The experiments in Fig. 1 taken together establish that δ-MnO_2 alone shows only modest OER activity, regardless of potential cycling of the film, and only when Mn^{3+} is introduced is enhanced OER activity observed.

In Situ X-Ray Absorption Spectroscopy. Fig. 2 shows the in situ X-ray absorption near-edge structure (XANES) spectra collected on an as-deposited δ-MnO_2 (birnessite) film activated by applying a two-step potential alternately between 1.1 and −0.4 V. The δ-MnO_2 film was electrodeposited in the in situ X-ray cell during XAS data collection. After sufficient material accrued, the film was realigned to the X-ray beam for optimal signal and then activated by applying the two-step potential 25 times. After each multistep cycle, an XAS spectrum was recorded (XANES spectra shown over a wider energy range are presented in *SI Appendix*, Fig. S5). The A0 XANES spectrum was collected on the as-deposited film, and subsequent spectra are shown for multiple cycles of 25 potential 1.1/−0.4 V steps terminating at the anodic potential (designated with A) or at a cathodic potential (designated with C).

The energy of the edge, determined from the inflection point as deduced from the maximum of the first derivative, shifts to lower energy on the application of the first multistep potential consistent with the generation of Mn^{3+} according to Eq. 4. Moreover, sequential spectra of cycles ending at the cathodic limiting potential exhibit a lower-energy absorption threshold than those terminating with the anodic limiting potential, giving rise to the sawtooth pattern shown in Fig. 2, *Inset*. Subsequent cycles ultimately converge to an absorption threshold of 6,549.75–6,550.0 eV (*SI Appendix*, Fig. S6), consistent with a

lower average oxidation state of manganese in activated films compared with the as-deposited film (XANES spectrum A0). The indication of a lower oxidation state in *SI Appendix*, Fig. S6 is consistent with the lower average oxidations state of +3.6–3.8 measured previously by coulometry (17) and CV and XPS studies (32, 33).

Fitting the first two peaks of the EXAFS data shown in *SI Appendix*, Fig. S7 for the cycles of Fig. 2 reveals a decrease in the Mn–O coordination number from predominantly six to four with cycling (Fig. 3A, red bars). Note that the primary Mn–Mn coordination number remains at two within the error limits of the fitting. As expected, the associated Mn–O and Mn–Mn bond lengths (Fig. 3B, red and blue bars, respectively) are relatively constant given that the activated film maintains primarily birnessite character (22). Furthermore, although M–O bonds in T_d sites tend to be shorter than that of Mn in O_h sites, this trend holds for Mn in the same oxidation state. The $Mn^{2+}(T_d)$ sites in hausmannite have an Mn–O bond length of 2.043 Å, while the adjacent $Mn^{3+}(O_h)$ sites have an average bond length of 2.046 Å. In birnessite, which makes up the majority of the material, the bond length is 1.89 Å, and thus, a bond length change of from 2.05 to 1.9 Å is the largest to be expected and is entirely within the error limits of our fitting. An Mn–O coordination number of four is typical of an Mn occupying a T_d site, which is supported by the increase in intensity of the preedge features visible in the XANES data near 6,542 eV after c1C (Fig. 2). Such an increase in the preedge data has been attributed to speciation of Mn in tetrahedral coordinated sites (51).

Raman Microspectroscopy. To gain further insight into the structural differences between δ-MnO$_2$ and δ-MnO$_2^{act}$ films, we carried out resonance Raman microspectroscopy with an excitation wavelength of 532 nm (Fig. 4). δ-MnO$_2$ displays a characteristic Raman spectrum in the range from 450 to 700 cm^{-1} with three dominant marker bands: a prominent Raman feature between 570 and 590 cm^{-1} corresponding to an in-plane Mn–O stretching vibration along the octahedral layers in δ-MnO$_2$ and two bands at ~500 and ~630–650 cm^{-1} associated with out-of-plane Mn–O vibrations perpendicular to the layers (52–56). All three bands are sensitive markers reporting on changes to the
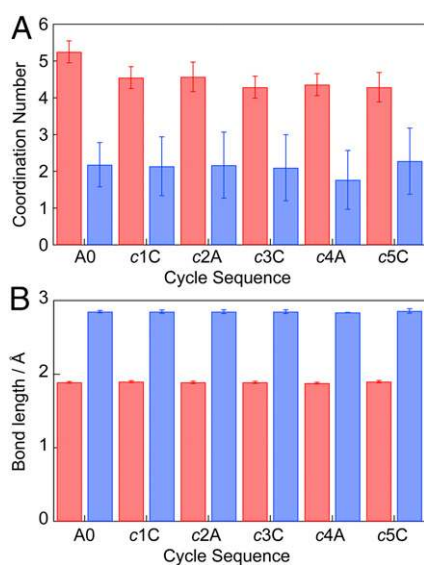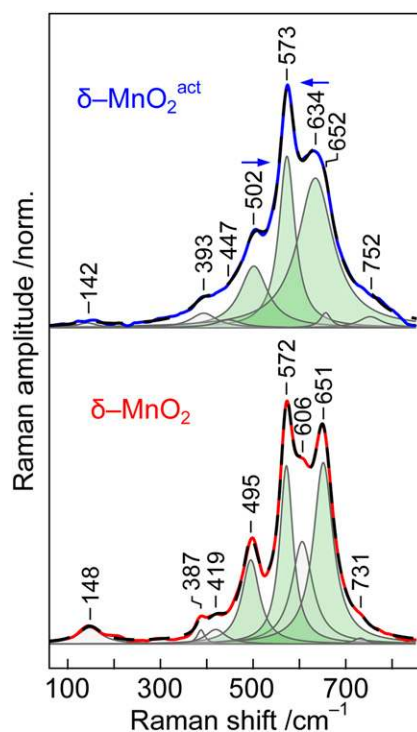

Fig. 4. Raman spectra of as-deposited δ-MnO$_2$ (red), activated δ-MnO$_2^{act}$ (blue) films, and corresponding spectral fit (black dashed). Individually fitted Lorentzian functions are shown in gray, with important marker bands highlighted in green as a visual aid. Blue arrows indicate frequency shifts compared with δ-MnO$_2$ of these marker bands.

oxidation states of octahedral Mn cations as well as the interlayer separation and structural distortions of the involved Mn–O environments (53, 54, 57). This specificity to the local structure of the [MnO$_6$] octahedral framework renders Raman spectroscopy useful to the investigation of the effects of the activation protocol for electrodeposited δ-MnO$_2$ films.

Fig. 4 shows the Raman spectra acquired for electrodeposited δ-MnO$_2$ (Fig. 4, red) and δ-MnO$_2^{act}$ (Fig. 4, blue). Various polymorphs of MnOx have been extensively studied in literature, and the δ-MnO$_2$ Raman spectrum (Fig. 4, red) is in excellent agreement with the previous literature reports of an in-plane Mn–O stretching vibration located at 572 cm^{-1} as well as out-of-plane Mn–O stretching vibrations at 495 and 651 cm^{-1} for the δ-MnO$_2$ polymorph (52, 56, 58). In addition, we observe a moderately intense band at 606 cm^{-1} as well as several bands with lower intensity at 148, 387, 419, and 731 cm^{-1}, all of which remain unassigned. We, therefore, concentrate only on the key marker bands in our analysis.

The δ-MnO$_2^{act}$ Raman spectrum (Fig. 4, blue) is significantly altered compared with that of δ-MnO$_2$. The prominent feature at 573 cm^{-1} in δ-MnO$_2^{act}$ is assigned to the in-plane Mn–O stretching mode by comparison with the corresponding 572-cm^{-1} band observed for δ-MnO$_2$. In contrast, the more intense out-of-plane Mn–O stretching vibration found at 651 cm^{-1} in δ-MnO$_2$ red-shifts in δ-MnO$_2^{act}$ to 634 cm^{-1}, and the other out-of-plane Mn–O stretching vibration blue-shifts to 502 cm^{-1}. Both out-of-plane stretching modes additionally show reduced intensity relative to the 573-cm^{-1} in-plane Mn–O stretching mode. A reduction in intensity is also observed for the low-frequency phonon mode at ~148 cm^{-1}, most likely indicative of a lower long-range order and higher strain present in the activated film (vide infra).

Fig. 3. (A) Mn–O (red) and Mn–Mn (blue) coordination numbers and (B) Mn–O (red) and Mn–Mn (blue) bond lengths as calculated from fitting parameters (*SI Appendix*, Table S1) of the EXAFS spectra (*SI Appendix*, Fig. S7). Cycle numbers are indicated as per Fig. 2.

Catalyst Structure and Oxidation Configuration. The catalysis mechanism underlying the superior performance of the activated δ-MnO_2 films (i.e., δ-MnO_2^{act}) can be understood by consideration of the electronic structure derived from the various local Mn–O ligand fields. The in situ XAS results reported here as well as ex situ X-ray pair distribution function analysis reported previously (22) indicate that the δ-MnO_2^{act} catalyst comprises both α-Mn_3O_4 hausmannite-like and δ-MnO_2 birnessite-like structures and does not contain local environments unique to any other known MnO_2 polymorph phase. Both structures comprise face-centered cubic oxygen frameworks with Mn occupying octahedral and tetrahedral interstitial sites (59) as illustrated in Fig. 5A. The XAS data presented in Fig. 2 establish the presence of Mn^{3+} and Mn^{4+} sites in the δ-MnO_2^{act} film but not the δ-MnO_2 film. Understanding the effect of Mn^{3+} on the electronic structure of δ-MnO_2^{act} is thus key to revealing the source of superior catalytic activity.

While the exact structure of an amorphous film is not amenable to a precise atomistic description, electronic behavior of the activated catalyst can be modeled by electronic titration of hausmannite α-Mn_3O_4 from its initial $Mn^{2.66+}$ average oxidation state to Mn^{4+}. As previously established, the activated film can only be reached via the hausmannite intermediate. Furthermore, as the α-Mn_3O_4 structure contains both the tetrahedral and octahedral Mn environments of interest (and no others), it provides a first-order approximation of the electronic structure of the catalyst, which can inform a discussion of the enhanced activity resulting from Mn^{3+} incorporation into a native Mn^{4+} oxidic lattice. Thus, oxidized α-Mn_3O_4 provides a tractable local

environment model of the oxidized, partial tetrahedral structure of δ-MnO_2^{act}.

The oxidation behavior of this structural model, shown in Fig. 5B, provides a picture of the relative stability of various oxidation states in the mixed tetrahedral/octahedral δ-MnO_2^{act} structure. From the initial hausmannite starting point, all tetrahedral Mn exists in the 2+ oxidation state, whereas octahedral Mn exists in the 3+ oxidation state. The valence band is dominated by a tetrahedral $Mn^{2+}(T_d)$ state, while the octahedral manganese ions are in a Jahn–Teller distorted, high-spin $Mn^{3+}(O_h)$ state, as expected for hausmannite (60). As the structure is oxidized, electrons are removed from the high-energy tetrahedral Mn states forming tetrahedral $Mn^{3+}(T_d)$ alongside the octahedral $Mn^{3+}(O_h)$ states. The next oxidation step removes electrons from the octahedral manganese sites, forming $Mn^{4+}(O_h)$. After three electrons per formula unit are removed from the Mn_3O_4 structure, all octahedral manganese is in the $Mn^{4+}(O_h)$ state, while all tetrahedral manganese ions are in the $Mn^{3+}(T_d)$ state. At this point, the valence band is dominated by oxygen states rather than tetrahedral $Mn^{3+}(T_d)$ states, indicating that the oxidation of tetrahedral $Mn^{3+}(T_d)$ is more difficult than that of oxygen. Consistent with this result, on further oxidation, electrons are extracted from O2p orbitals, while the tetrahedral sites remain as $Mn^{3+}(T_d)$ (Fig. 5B). Indeed, after the onset of oxygen oxidation, some of the octahedral Mn regains some $Mn^{3+}(O_h)$ character. Thus, with the observation of the energy ordering of an O valence band to higher energy than that of manganese valence bands, we conclude that any tetrahedral Mn in the activated film would remain as $Mn^{3+}(T_d)$ even under highly oxidizing
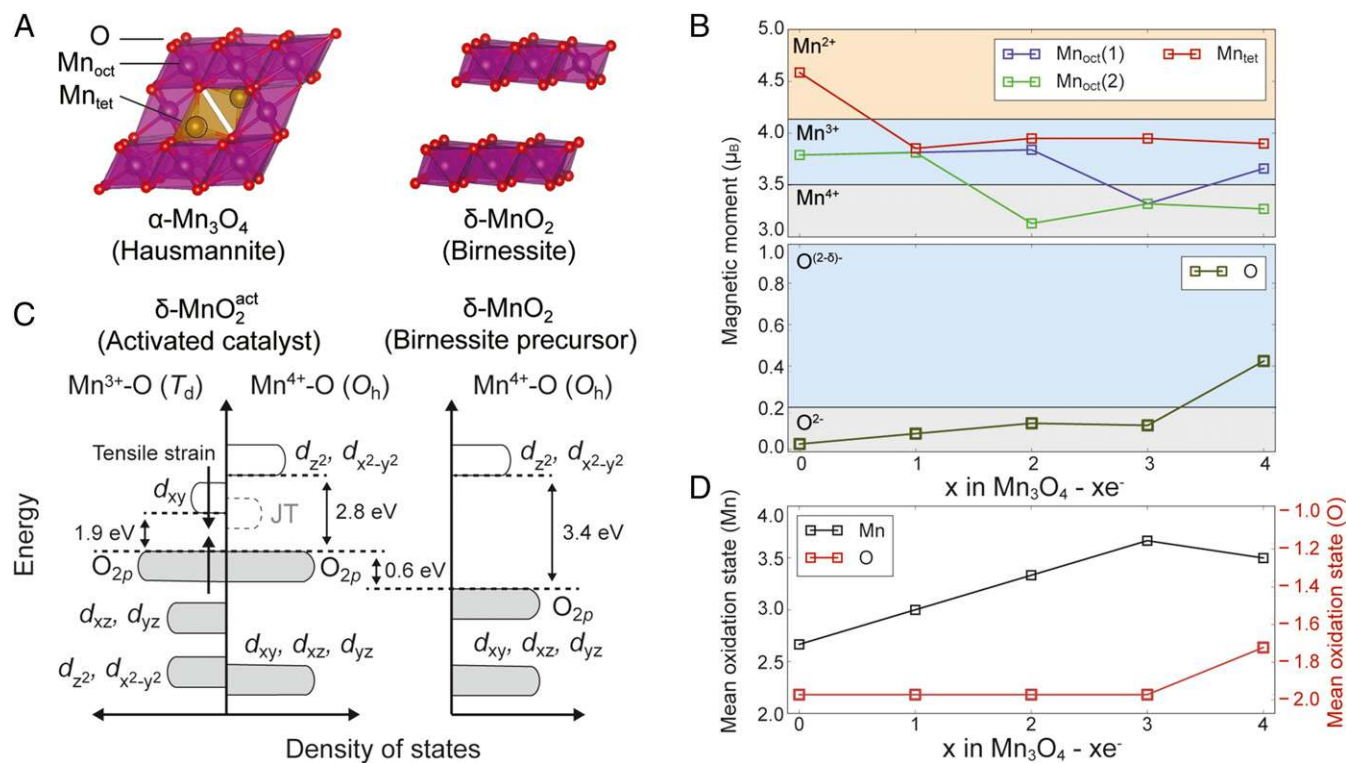

Fig. 5. Electronic structure of the activated catalyst based on an oxidized α-Mn_3O_4 hausmannite structure as a model system containing both octahedral and tetrahedral Mn–O environments. (*A*) Schematic representation of the α-Mn_3O_4 hausmannite and δ-MnO_2 structures illustrating their common underlying face-centered cubic oxygen framework and similarity in octahedral Mn structure. The unique tetrahedral Mn sites in α-Mn_3O_4 are highlighted. (*B*) Evolution of oxidation states of Mn and O as electrons are removed from the α-Mn_3O_4 model system. Oxidation states are derived from the values of characteristic atom-projected magnetic moments according to typical values observed for computed manganese oxides and hydroxides. (*C*) Schematic of the band structure of the activated catalyst system derived from the "α-Mn_3O_4– 3e⁻" model. The T_d and O_h sections of the band diagram represent tetrahedral and octahedral Mn environments, while the Jahn–Teller orbital depicts the relative position of the O_h LUMO accounting for structural relaxation through Jahn–Teller distortion. (*D*) Average valence of Mn and O as a function of oxidation level as indicated by the electronically titrated α-Mn_3O_4 model.

conditions, forcing oxygen electrons to the valence band edge even for an average Mn oxidation state below Mn^{4+} as is observed in the in situ XAS data shown in Fig. 2. This observation suggests that the activated catalyst described here operates via a similar mechanism to that proposed by Smith et al. (30): the suppression of Mn^{4+} formation by particular bonding structure enables the formation of oxygen holes competitively with $Mn^{3+/4+}$ oxidation.

A schematic illustration of the electronic structure of the activated film, derived from the fully oxidized α-Mn_3O_4 structural model, is given in Fig. 5C. Consistent with the results of the electronic titration calculation (Fig. 5B), the highest occupied molecular orbital (HOMO) is dominated by O2p states, while the lowest unoccupied molecular orbital (LUMO) is composed of antibonding states of tetrahedral $Mn^{3+}(T_d)$. Octahedral Mn is oxidized from $Mn^{3+}(O_h)$ to $Mn^{4+}(O_h)$ at a higher potential than that of the tetrahedral $Mn^{2+/3+}(T_d)$ transition; the origin of this order of oxidation potentials is in the stabilization of octahedral $Mn^{3+}(O_h)$ by Jahn–Teller distortion. In the undistorted octahedral environment found with $Mn^{4+}(O_h)$, the unoccupied antibonding e_g^* state is shifted up in energy and is above the LUMO of tetrahedral $Mn^{3+}(T_d)$. A more subtle effect on energy ordering arises from the impact of local tensile strain, as adjacent tetrahedral and octahedral environments are oxidized. As $Mn^{3+}(T_d)$ states initially form from $Mn^{2+}(T_d)$, the average T_d Mn–O bond length decreases from 2.04 to 1.98 Å. On oxidation of the nearby octahedral environments to $Mn^{4+}(O_h)$, the strong Mn–O bonding in the octahedra stretches the bonds in the tetrahedral environment, increasing the average T_d Mn–O bond length to 2.16 Å. This local strain confers more ionic character to the T_d Mn–O interaction and lowers the energy of the antibonding T_d LUMO, further decreasing the energy gap between the occupied O2p states and unoccupied Mn states. The red shift in the ultraviolet-visible spectrum of δ-MnO_2^{act} compared with δ-MnO_2 (*SI Appendix*, Fig. S2) is consistent with this prediction of a reduced HOMO–LUMO gap. This decrease in energy gap leads to a further facilitation of the OER, as these stabilized empty states accept the electrons released from reductive elimination of O_2.

An important feature of the electronic structure of the activated catalyst is the relative position of the HOMO oxygen band vs. that of pure δ-MnO_2. We align the band structures of the two structures using characteristic features of the $Mn^{4+}(O_h)$ environment present in both structures, effectively measuring the position of the occupied oxygen states with respect to the $Mn(O_h)$ t_{2g} levels shared by both structures. This method yields an informative model of the differences in the electronic states of the two materials but inherently neglects the impact of structural features beyond the nearest neighbor cation–anion coordination shell. Nonetheless, based on this alignment (*SI Appendix*, Fig. S8), we can conclude that the activated catalyst contains higher energy oxygen states than pure δ-MnO_2 birnessite, with the oxygen band in the catalyst extending up to 0.6 eV above the Fermi level of birnessite. Note that, while the absolute values of the HOMO–LUMO gaps may be overestimated by the computational methodology used here, their relative values are reliable. The presence of these higher-energy oxygen states can be rationalized by the significant tensile strain experienced by oxygen bridging Mn^{3+} and Mn^{4+} environments, as this strain decreases the Mn–O orbital overlap and destabilizes the bonded state.

Discussion

The strong evidence of tetrahedral Mn in the fully oxidized and activated δ-MnO_2^{act} film gives valuable insight into the electronic structure of the activated catalyst and provides a rationale for superior performance in the presence of Mn^{3+} in enhancing OER catalysis with MnO_2 polymorphs. Qualitatively, Mn^{3+} is well-known to promote oxygen evolution (17, 61–64) but has

been difficult to isolate in neutral and acidic conditions (65). Based on the Mn Pourbaix diagram (66), Mn_2O_3 and MnOOH may only be stable under alkaline conditions, while under acidic conditions, the only stable oxidation states of manganese are Mn^{2+} and Mn^{4+}. Correspondingly, Mn^{3+}, if formed within an oxide lattice, typically disproportionates to form Mn^{2+} and Mn^{4+} below pH 9 (62, 63, 65, 67). One unique result reported here is that Mn in tetrahedral sites is kinetically trapped, and in a fully oxidized structure, the tetrahedral Mn is forced to remain as $Mn^{3+}(T_d)$. Indeed, in the oxidized δ-MnO_2^{act} film, where all octahedral Mn is fully oxidized to $Mn^{4+}(O_h)$ and tetrahedral Mn is fully oxidized to $Mn^{3+}(T_d)$, no disproportionation reaction is possible, and it is not observed. This result is supported by the experimental XPS studies that show a persistent average Mn oxidation state of $Mn^{3.6+-3.8+}$ (22), with only Mn^{3+} and Mn^{4+} in the fully oxidized film under anodic conditions, as well as the EXAFS studies revealing a decrease in the Mn–O coordination number for the activated film.

The persistence of the metastable tetrahedral Mn species in the oxidized film is consistent with the migration behavior of Mn in rock salt-derived oxides, such as hausmannite and birnessite. Previous studies have found that Mn migration through the structure proceeds through hops between adjacent T_d and O_h sites. However, Mn^{2+} is the only species that is able to migrate between these T_d and O_h sites in the structure, while Mn^{3+} and Mn^{4+} are immobile (68, 69). Thus, Mn^{3+} "migrates" only by disproportionating into Mn^{2+} and Mn^{4+}, after which the Mn^{2+} ion moves through the structure (69). As no disproportionation reaction is possible in the fully oxidized δ-MnO_2^{act} film, we speculate that the Mn is kinetically locked in its metastable T_d site.

The Raman data support the computational titration of hausmannite presented in Fig. 5B. Mn^{3+} is kinetically trapped in the interlayer T_d sites, with the octahedral $[MnO_6]$ framework remaining largely that of birnessite-like octahedral Mn^{4+}, since the 572-cm^{-1} Mn–O stretching vibration of δ-MnO_2 (Fig. 4, red) remains unchanged on activation (Fig. 4, blue). In contrast, frequency shifts associated with out-of-plane vibrations (495 and 651 cm^{-1}) are intimately related to the interlayer geometry. Red shifts of up to 15 cm^{-1} have been reported for the 651-cm^{-1} mode in δ-MnO_2 and have been attributed to a contraction of the $[MnO_6]$ interlayer spacing due to reduced interlayer repulsion of the $[MnO_6]$ octahedra (54). Furthermore, similar spectral changes were also observed during electrochemical potential sweeps and attributed to a phase transition from initially hexagonal to monoclinic (57). The observed Raman shifts and relative intensity changes of the 502- and 634-cm^{-1} bands in MnO_2^{act}, therefore, provide evidence on changes to the interlayer separation due to the existence of interlayer Mn^{3+} ions that persist even after a final anodic potential pulse, consistent with theoretical modeling.

In combination with our XAS results and theoretical modeling, we formulate a structural picture of the MnO_2^{act} catalyst film, in which the octahedral $[MnO_6]$ framework is structurally largely robust when interlayer Mn^{3+} cations are present. The Raman shift of the out-of-plane modes together with the lowering of the Mn oxidation number reported by XAS supports the contention that the role of the activation procedure is to generate interlayer Mn^{3+} ions, which in turn, cause strain of the initial layered birnessite lattice. This strain establishes most likely the formation of a partial 3D hausmannite-like structure, in which Mn^{3+} ions occupy tetrahedral sites, as suggested by the lowering of the Mn–O coordination number and theoretical modeling. Consequently, the film maintains $Mn^{3+}(T_d)$ character on onset of OER.

The electronic structure of the activated film, shown in Fig. 5C, suggests a mechanistic role for $Mn^{3+}(T_d)$ states in driving oxygen evolution through both the generation of reactive oxygen states and a decreased HOMO–LUMO gap. The activated

film has the general structure of a charge-transfer insulator, with the HOMO dominated by particularly weakly bound O2p states, while the LUMO consists of antibonding states within the $Mn^{3+}(T_d)$ environment. Such an electronic structure has been generally correlated to high oxygen evolution activity (70). Mechanistically, in such a structure, electronic excitations create oxygen holes ($Mn^n-O \rightarrow Mn^{n-1}-O\cdot$), forming highly reactive oxyl radicals, which are known to be critical intermediates in the proton-coupled electron transfer transformation of H_2O to O_2 (71–76) and in the proposal of reductive coupling (77, 78) and excess charging in Li batteries (79). The generation of oxyl radicals resulting from a high lying O2p valence band, with the population of oxygen radicals inversely proportional to the size of the HOMO–LUMO energy gap, is an emerging precept for the origin of enhanced OER activity in oxidic metal catalysts (80). While pristine birnessite δ-MnO_2 has similar charge-transfer character to the activated film, the oxygen in δ-MnO_2 is significantly more bound than in the activated catalyst as evidenced by the lower absolute energy of the oxygen band. Furthermore, the HOMO–LUMO gap is calculated to be between 2.8 and 3.4 eV, which results in a very small population of reactive oxygen radicals. In contrast, the metastable $Mn^{3+}(T_d)$ states of δ-MnO_2^{act} create low-lying metal states, with a calculated HOMO–LUMO gap of 1.9 eV, which can be further decreased by local tensile strains likely present around these tetrahedral sites.

The redox behavior of the δ-MnO_2^{act} catalyst material is similar to that observed in disordered Li-excess materials, which have recently received significant attention as high-capacity cathodes for Li ion batteries. The competition between $Mn^{3+/4+}$ and oxygen oxidation found in the δ-MnO_2^{act} catalyst is analogous to the activation of oxygen redox preferentially to transition metal oxidation in Li-excess cathodes. In both cases, the redox behavior is controlled by unique local bonding environments, with strained metal–oxygen bonds in this δ-MnO_2 material and poorly hybridized Li–O–Li environments in Li-excess cathodes leading to the formation of reactive oxygen states (79, 81). Similarly, transition metal oxidation is suppressed in both cases by constraining metal–oxygen bond lengths to that of the reduced state (77, 82). The result of these mechanisms is a promotion of oxygen evolution from the disordered metastable material, thus leading to enhanced OER activity.

Conclusion

The enhanced OER activity of MnO_2 polymorph OER catalysts is known to be derived from the presence of Mn^{3+} ions, where the suppression of Mn^{3+} oxidation to Mn^{4+} by structural constraints has been proposed as a key step in enabling oxygen hole accumulation and the reductive elimination of O_2 (39, 40). We find that the incorporation of Mn^{3+}, which typically disproportionates in oxide lattices, is enabled by the comproportionation of Mn^{4+} in the form of MnO_2 and Mn^{2+} in the form of $Mn(OH)_2$. The kinetic trapping of Mn^{3+} is thus only possible via this comproportionation effect, which requires the generation of OH^- and the presence of Mn^{2+}. Further examination of the activated structure yields insights extending beyond the observation of Mn^{3+} valency, promoting higher catalytic turnover. Raman microspectroscopy provides evidence for a locally strained lattice due to the presence of interlayer Mn^{3+} cations. In situ XANES and EXAFS further show that Mn^{3+} is most likely coordinated by a T_d ligand field in the activated films. In combination with computational modeling, these results suggest a local 3D hausmannite-like structure that produces an HOMO level primarily dominated by O2p valence states and unoccupied metal-based LUMO states with an attenuated HOMO–LUMO gap. In this light, our activated catalyst is similar to the mechanism of Mn^{4+} suppression in Mn_2O_3 and γ-MnOOH as proposed by Smith et al. (30): the Mn cations trapped in T_d sites are unable to form Mn^{4+} and thus, induce a reordering of Mn-d and O2p states, facilitating oxygen hole formation. These factors contribute to enhanced OER activity by facilitating oxyl radical formation for reductive coupling to produce oxygen, providing crucial design principles for the improvement of OER activity in metal oxidic catalysts.

1. Nocera DG (2006) On the future of global energy. *Daedalus* 135:112–115.
2. Chu S, Majumdar A (2012) Opportunities and challenges for a sustainable energy future. *Nature* 488:294–303.
3. Cook TR, et al. (2010) Solar energy supply and storage for the legacy and nonlegacy worlds. *Chem Rev* 110:6474–6502.
4. Lewis NS, Nocera DG (2006) Powering the planet: Chemical challenges in solar energy utilization. *Proc Natl Acad Sci USA* 103:15729–15735.
5. Hammes-Schiffer S (2009) Theory of proton-coupled electron transfer in energy conversion processes. *Acc Chem Res* 42:1881–1889.
6. Surendranath Y, Nocera DG (2011) Oxygen evolution reaction chemistry of oxide-based electrodes. *Prog Inorg Chem* 57:505–560.
7. Kanan MW, Nocera DG (2008) In situ formation of an oxygen-evolving catalyst in neutral water containing phosphate and Co2+. *Science* 321:1072–1075.
8. Surendranath Y, Dincă M, Nocera DG (2009) Electrolyte-dependent electrosynthesis and activity of cobalt-based water oxidation catalysts. *J Am Chem Soc* 131:2615–2620.
9. Surendranath Y, Kanan MW, Nocera DG (2010) Mechanistic studies of the oxygen evolution reaction by a cobalt-phosphate catalyst at neutral pH. *J Am Chem Soc* 132:16501–16509.
10. Gerken JB, et al. (2011) Electrochemical water oxidation with cobalt-based electrocatalysts from pH 0-14: The thermodynamic basis for catalyst structure, stability, and activity. *J Am Chem Soc* 133:14431–14442.
11. Klingan K, et al. (2014) Water oxidation by amorphous cobalt-based oxides: Volume activity and proton transfer to electrolyte bases. *ChemSusChem* 7:1301–1310.
12. Corrigan DA (1987) The catalysis of the oxygen evolution reaction by iron impurities in thin film nickel oxide electrodes. *J Electrochem Soc* 134:377–384.
13. Dincă M, Surendranath Y, Nocera DG (2010) Nickel-borate oxygen-evolving catalyst that functions under benign conditions. *Proc Natl Acad Sci USA* 107:10337–10341.
14. Bediako DK, Surendranath Y, Nocera DG (2013) Mechanistic studies of the oxygen evolution reaction mediated by a nickel-borate thin film electrocatalyst. *J Am Chem Soc* 135:3662–3674.
15. Trotochaud L, Young SL, Ranney JK, Boettcher SW (2014) Nickel-iron oxyhydroxide oxygen-evolution electrocatalysts: The role of intentional and incidental iron incorporation. *J Am Chem Soc* 136:6744–6753.
16. Görlin M, et al. (2017) Tracking catalyst redox states and reaction dynamics in Ni–Fe oxyhydroxide oxygen evolution reaction electrocatalysts: The role of catalyst support and electrolyte pH. *J Am Chem Soc* 139:2070–2082.
17. Huynh M, Bediako DK, Nocera DG (2014) A functionally stable manganese oxide oxygen evolution catalyst in acid. *J Am Chem Soc* 136:6002–6010.
18. Huynh M, Bediako DK, Liu Y, Nocera DG (2014) Nucleation and growth mechanisms of an electrodeposited manganese oxide catalyst at near-neutral pH. *J Phys Chem C* 118:17142–17152.
19. Kang D, et al. (2015) Electrochemical synthesis of photoelectrodes and catalysts for use in solar water splitting. *Chem Rev* 115:12839–12887.
20. Roger I, Symes MD (2016) First row transition metal catalysts for solar-driven water oxidation produced by electrodeposition. *J Mater Chem A* 4:6724–6741.
21. Costentin C, Nocera DG, Brodsky CN (2017) Multielectron, multisubstrate molecular catalysis of electrochemical reactions: Formal kinetic analysis in the total catalysis regime. *Proc Natl Acad Sci USA* 114:11303–11308.
22. Huynh M, Shi C, Billinge SJL, Nocera DG (2015) Nature of activated manganese oxide for oxygen evolution. *J Am Chem Soc* 137:14887–14904.
23. Bloor LG, Molina PI, Symes MD, Cronin L (2014) Low pH electrolytic water splitting using earth-abundant metastable catalysts that self-assemble in situ. *J Am Chem Soc* 136:3304–3311.
24. Frydendal R, Paoli EA, Chorkendorff I, Rossmeisl J, Stephens IEL (2015) Toward an active and stable catalyst for oxygen evolution in acidic media: Ti-stabilized MnO2. *Adv Energy Mater* 5:1500991.

CHEMISTRY

25. Jones RJR, et al. (2015) Parallel electrochemical treatment system and application for identifying acid-stable oxygen evolution electrocatalysts. *ACS Comb Sci* 17:71–75.

26. Meng Y, et al. (2014) Structure-property relationship of bifunctional MnO2 nanostructures: Highly efficient, ultra-stable electrochemical water oxidation and oxygen reduction reaction catalysts identified in alkaline media. *J Am Chem Soc* 136:11452–11464.

27. Morita M, Iwakura C, Tamura H (1979) The anodic characteristics of massive manganese oxide electrode. *Electrochim Acta* 24:357–362.

28. Najafpour MM, et al. (2013) Nano-size layered manganese-calcium oxide as an efficient and biomimetic catalyst for water oxidation under acidic conditions: Comparable to platinum. *Dalton Trans* 42:5085–5091.

29. Robinson DM, et al. (2013) Photochemical water oxidation by crystalline polymorphs of manganese oxides: Structural requirements for catalysis. *J Am Chem Soc* 135:3494–3501.

30. Smith PF, et al. (2016) Coordination geometry and oxidation state requirements of corner-sharing MnO6 octahedra for water oxidation catalysis: An investigation of manganite (γ-MnOOH). *ACS Catal* 6:2089–2099.

31. Takashima T, Hashimoto K, Nakamura R (2012) Inhibition of charge disproportionation of MnO2 electrocatalysts for efficient water oxidation under neutral conditions. *J Am Chem Soc* 134:18153–18156.

32. Zaharieva I, et al. (2012) Electrosynthesis, functional, and structural characterization of a water-oxidizing manganese oxide. *Energy Environ Sci* 5:7081–7089.

33. Gorlin Y, et al. (2013) In situ X-ray absorption spectroscopy investigation of a bifunctional manganese oxide catalyst with high activity for electrochemical water oxidation and oxygen reduction. *J Am Chem Soc* 135:8525–8534.

34. Ravel B, Newville M (2005) ATHENA, ARTEMIS, HEPHAESTUS: Data analysis for X-ray absorption spectroscopy using IFEFFIT. *J Synchrotron Radiat* 12:537–541.

35. Ravel B (2015) ATHENA: XAS data processing. Available at bruceravel.github.io/demeter/documents/Athena/index.html. Accessed April 1, 2015.

36. Hybertsen MS, Louie SG (1986) Electron correlation in semiconductors and insulators: Band gaps and quasiparticle energies. *Phys Rev B Condens Matter* 34:5390–5413.

37. Seo D-H, Urban A, Ceder G (2015) Calibrating transition-metal energy levels and oxygen bands in first-principles calculations: Accurate prediction of redox potentials and charge transfer in lithium transition-metal oxides. *Phys Rev B* 92:115118.

38. Heyd J, Scuseria GE, Ernzerhof M (2003) Hybrid functionals based on a screened coulomb potential. *J Chem Phys* 118:8207–8215.

39. Perdew JP, Burke K, Ernzerhof M (1996) Generalized gradient approximation made simple. *Phys Rev Lett* 77:3865–3868.

40. Lany S (2013) Band-structure calculations for the 3d transition metal oxides in GW. *Phys Rev B* 87:085112.

41. Xu H, Xu S, Wang H, Yan H (2005) Characterization of hausmannite Mn3O4 thin films by chemical bath deposition. *J Electrochem Soc* 152:C803–C807.

42. Dubal D, et al. (2009) A novel chemical synthesis of interlocked cubes of hausmannite Mn3O4 thin films for supercapacitor application. *J Alloys Compd* 484:218–221.

43. Hosny NM, Dahshan A (2012) Facile synthesis and optical band gap calculation of Mn3O4 nanoparticles. *Mater Chem Phys* 137:637–643.

44. Persson C, Zhao YJ, Lany S, Zunger A (2005) N-type doping of CuInSe2 and CuGaSe2. *Phys Rev B* 72:035211.

45. Raebiger H, Lany S, Zunger A (2008) Charge self-regulation upon changing the oxidation state of transition metals in insulators. *Nature* 453:763–766.

46. Kresse G, Furthmuller J (1996) Efficiency of *ab-initio* total energy calculations for metals and semiconductors using a plane-wave basis set. *Comput Mater Sci* 6:15–50.

47. Kresse G, Joubert D (1999) From ultrasoft pseudopotentials to the projector augmented-wave method. *Phys Rev B* 59:1758–1775.

48. Belsky A, Hellenbrandt M, Karen VL, Luksch P (2002) New developments in the Inorganic Crystal Structure Database (ICSD): Accessibility in support of materials research and design. *Acta Crystallogr B* 58:364–369.

49. Kitchaev DA, et al. (2016) Energetics of MnO2 polymorphs in density functional theory. *Phys Rev B* 93:045132.

50. Therese GHA, Kamath PV (2000) Electrochemical synthesis of metal oxides and hydroxides. *Chem Mater* 12:1195–1204.

51. Chalmin E, Farges F, Brown GE (2008) A pre-edge analysis of Mn K-edge XANES spectra to help determine the speciation of manganese in minerals and glasses. *Contrib Mineral Petrol* 157:111–126.

52. Julien C, Massot M (2002) Spectroscopic studies of the local structure in positive electrodes for lithium batteries. *Phys Chem Chem Phys* 4:4226–4235.

53. Julien C, et al. (2003) Raman spectra of birnessite manganese dioxides. *Solid State Ion* 159:345–356.

54. Chen D, et al. (2015) Probing the charge storage mechanism of a pseudocapacitive MnO2 electrode using in operando Raman spectroscopy. *Chem Mater* 27:6608–6619.

55. Yang L, et al. (2016) Investigation into the origin of high stability of δ-MnO2 pseudocapacitive electrode using operando Raman spectroscopy. *Nano Energy* 30:293–302.

56. Cheng S, et al. (2014) Phase evolution of an alpha MnO2-based electrode for pseudocapacitors probed by in operando Raman spectroscopy. *Nano Energy* 9:161–167.

57. Hsu Y-K, Chen Y-C, Lin Y-G, Chen L-C, Chen K-H (2011) Reversible phase transformation of MnO2 nanosheets in an electrochemical capacitor investigated by *in situ* Raman spectroscopy. *Chem Commun (Camb)* 47:1252–1254.

58. Julien CM, Massot M, Poinsignon C (2004) Lattice vibrations of manganese oxides. Part I. Periodic structures. *Spectrochim Acta A Mol Biomol Spectrosc* 60:689–700.

59. Kitchaev DA, Dacek ST, Sun W, Ceder G (2017) Thermodynamics of phase selection in MnO2 framework structures through alkali intercalation and hydration. *J Am Chem Soc* 139:2672–2681.

60. Jensen GB, Nielsen OV (1974) Magnetic-structure of Mn3O4 (hausmannite) between K and Neel point, 41 K. *J Phys Chem* 7:409–424.

61. Najafpour MM, Tabrizi MA, Haghighi B, Govindjee (2012) A manganese oxide with phenol groups as a promising structural model for water oxidizing complex in Photosystem II: A 'golden fish'. *Dalton Trans* 41:3906–3910.

62. Indra A, et al. (2013) Active mixed-valent MnO(x) water oxidation catalysts through partial oxidation (corrosion) of nanostructured MnO particles. *Angew Chem Int Ed Engl* 52:13206–13210.

63. Ryabova A, et al. (2016) Rationalizing the influence of the Mn(IV)/Mn(III) redox transition on the electrocatalytic activity of manganese oxides in the oxygen reduction reaction. *Electrochim Acta* 187:161–172.

64. Jin K, et al. (2017) Mechanistic investigation of water oxidation catalyzed by uniform, assembled MnO nanoparticles. *J Am Chem Soc* 139:2277–2285.

65. Takashima T, Hashimoto K, Nakamura R (2012) Mechanisms of pH-dependent activity for water oxidation to molecular oxygen by MnO2 electrocatalysts. *J Am Chem Soc* 134:1519–1527.

66. Pourbaix M (1974) *Atlas of Electrochemical Equilibria in Aqueous Solutions* (National Association of Corrosion Engineers, Houston), 2nd Ed.

67. Seo H, et al. (2017) Water oxidation mechanism for 3d transition metal oxide catalysts under neutral condition. *J Korean Ceram Soc* 54:1–8.

68. Reed J, Ceder G, Van Der Ven A (2001) Layered-to-spinel phase transition in LixMnO2. *Electrochem Solid State Lett* 4:A78–A81.

69. Kim S, et al. (2016) On the mechanism of crystal water insertion during anomalous spinel-to-birnessite phase transition. *Chem Mater* 28:5488–5494.

70. Grimaud A, et al. (2017) Activating lattice oxygen redox reactions in metal oxides to catalyse oxygen evolution. *Nat Chem* 9:457–465.

71. Wang LP, Troy VV (2011) Direct-coupling O2 bond forming a pathway in cobalt oxide water oxidation catalysts. *J Phys Chem Lett* 2:2200–2204.

72. Yang X, Baik MH (2006) cis,cis-[(bpy)2RuVO]2O4+ catalyzes water oxidation formally via in situ generation of radicaloid RuIV-O. *J Am Chem Soc* 128:7476–7485.

73. Jiang Y, et al. (2013) Promoting the activity of catalysts for the oxidation of water with bridged dinuclear ruthenium complexes. *Angew Chem Int Ed Engl* 52:3398–3401.

74. Zhang M, de Respinis M, Frei H (2014) Time-resolved observations of water oxidation intermediates on a cobalt oxide nanoparticle catalyst. *Nat Chem* 6:362–367.

75. Weinberg DR, et al. (2012) Proton-coupled electron transfer. *Chem Rev* 112:4016–4093.

76. Brodsky CN, et al. (2017) In situ characterization of cofacial Co(IV) centers in Co4O4 cubane: Modeling the high-valent active site in oxygen-evolving catalysts. *Proc Natl Acad Sci USA* 114:3855–3860.

77. Sathiya M, et al. (2013) Reversible anionic redox chemistry in high-capacity layered-oxide electrodes. *Nat Mater* 12:827–835.

78. Saubanere M, McCalla E, Tarascon JM, Doublet ML (2016) The intriguing question of anionic redox in high-energy density cathodes for Li-ion batteries. *Energy Environ Sci* 9:984–991.

79. Seo DH, et al. (2016) The structural and chemical origin of the oxygen redox activity in layered and cation-disordered Li-excess cathode materials. *Nat Chem* 8:692–697.

80. Li N, et al. (2017) Influence of iron doping on tetravalent nickel content in catalytic oxygen evolving films. *Proc Natl Acad Sci USA* 114:1486–1491.

81. Luo K, et al. (2016) Charge-compensation in 3d-transition-metal-oxide intercalation cathodes through the generation of localized electron holes on oxygen. *Nat Chem* 8:684–691.

82. Lee J, et al. (2018) Reversible Mn^{2+}/Mn^{4+} double redox in lithium-excess cathode materials. *Nature* 556:185–190.